

A FLUX-LIMITED SAMPLE OF $Z \sim 1$ $\text{Ly}\alpha$ EMITTING GALAXIES IN THE CDFS^{1,2}

A. J. BARGER,^{3,4,5} L. L. COWIE,⁵ I. G. B. WOLD³

Accepted by The Astrophysical Journal

ABSTRACT

We describe a method for obtaining a flux-limited sample of $\text{Ly}\alpha$ emitters from *GALEX* grism data. We show that the multiple *GALEX* grism images can be converted into a three-dimensional (two spatial axes and one wavelength axis) data cube. The wavelength slices may then be treated as narrowband images and searched for emission-line galaxies. For the *GALEX* NUV grism data, the method provides a $\text{Ly}\alpha$ flux-limited sample over the redshift range $z = 0.67 - 1.16$. We test the method on the *Chandra* Deep Field South field, where we find 28 $\text{Ly}\alpha$ emitters with faint continuum magnitudes ($\text{NUV} > 22$) that are not present in the *GALEX* pipeline sample. We measure the completeness by adding artificial emitters and measuring the fraction recovered. We find that we have an 80% completeness above a $\text{Ly}\alpha$ flux of $10^{-15} \text{ erg cm}^{-2} \text{ s}^{-1}$. We use the UV spectra and the available X-ray data and optical spectra to estimate the fraction of active galactic nuclei in the selection. We report the first detection of a giant $\text{Ly}\alpha$ blob at $z < 1$, though we find that these objects are much less common at $z = 1$ than at $z = 3$. Finally, we compute limits on the $z \sim 1$ $\text{Ly}\alpha$ luminosity function and confirm that there is a dramatic evolution in the luminosity function over the redshift range $z = 0 - 1$.

Subject headings: cosmology: observations — galaxies: distances and redshifts — galaxies: evolution — galaxies: starburst — galaxies: active

1. INTRODUCTION

$\text{Ly}\alpha$ is the only emission line that we can detect in the highest redshift ($z > 6$) galaxies, making it the only probe of the internal structure of these galaxies and one of the few diagnostic tools for studying the intergalactic gas. However, separating the internal and external effects will always be difficult at these redshifts. Thus, to determine the intrinsic $\text{Ly}\alpha$ properties of galaxies, we need to study lower redshift samples where the galaxy structure can be separated from the effects of the intergalactic medium.

Recently, substantial samples of $z \sim 0.2 - 0.4$ $\text{Ly}\alpha$ emitters (LAEs) and a small number of $z \sim 1$ LAEs have been found with the *Galaxy Evolution Explorer* (*GALEX*; Martin et al. 2005) grism spectrographs. The pipeline extractions for the grism spectrographs provide spectra to a fixed limiting near-ultraviolet (NUV) magnitude that can be searched for $\text{Ly}\alpha$ emission lines (Deharveng et al. 2008; Cowie et al. 2010). The procedure enables the selection of a substantial sample of sources that can be compared to the high-redshift LAEs. Since the selection process is based on finding $\text{Ly}\alpha$ in the UV-continuum selected *GALEX* sources, it is most analogous to locating LAEs in the Lyman break galaxy (LBG) population using spectroscopy (e.g., Shapley et al. 2003).

The advent of these low-redshift LAE catalogs has been very exciting, and many follow-up papers have been written (e.g., Finkelstein et al. 2009a, 2009b; Atek et al. 2009; Scarlata et al. 2009; Cowie et al. 2011). How-

ever, because the *GALEX* grism pipeline only includes objects whose UV continuum magnitudes are bright enough to generate measurable continuum spectra, only a fraction of the emission-line objects at these redshifts are detected. In particular, strong emitters with high equivalent widths (EWs) may have emission lines that are detectable but continuum magnitudes that fall below the continuum threshold.

Moreover, because the samples have both a continuum and an emission-line selection, it is not straightforward to compute the LAE luminosity functions (see the extensive discussions in Deharveng et al. 2008 and Cowie et al. 2010). Thus, ad hoc assumptions about the invariance of the EW distribution as a function of continuum magnitude need to be made, even though they may not be correct.

Fortunately, it is possible to detect directly the excluded emitters by re-extracting the *GALEX* data. In this paper, we show how to find “orphan” emission lines (e.g., Straughn et al. 2008; Keel et al. 2009) and how to generate a flux-limited $\text{Ly}\alpha$ emission-line sample. We refer to this approach as a data cube search. First, we extract a spectrum for every spatial pixel in the *GALEX* fields. Next, we form a three-dimensional data cube, analogous to that produced by an integral field unit, with two spatial axes and a third wavelength axis. Finally, we search the wavelength slices in these data cubes for emitters.

An alternative procedure is to use the deep broadband *GALEX* images to develop a target list of galaxies fainter than those used in the pipeline and then to extract the

¹Based in part on data obtained from the Multimission Archive at the Space Telescope Science Institute (MAST). STScI is operated by the Association of Universities for Research in Astronomy, Inc., under NASA contract NAS5-26555. Support for MAST for non-HST data is provided by the NASA Office of Space Science via grant NAG5-7584 and by other grants and contracts.

²This research used the facilities of the Canadian Astronomy Data Centre operated by the National Research Council of Canada with the support of the Canadian Space Agency.

³Department of Astronomy, University of Wisconsin-Madison, 475 North Charter Street, Madison, WI 53706.

⁴Department of Physics and Astronomy, University of Hawaii, 2505 Correa Road, Honolulu, HI 96822.

⁵Institute for Astronomy, University of Hawaii, 2680 Woodlawn Drive, Honolulu, HI 96822.

spectra of these objects. However, since this approach still introduces a pre-selection (which must be included and modeled in any interpretation and may omit extreme EW emitters), we prefer to use the data cube approach.

In order to fully understand the LAEs that we find, we need a wealth of ancillary data. In particular, the key requirement is as extensive a set of redshift measurements as possible. Thus, for this paper, we focus on the intensively studied *Chandra* Deep Field South (CDFS; Giacconi et al. 2002) region, where we can use both existing optical spectroscopy to confirm the UV identifications of the Ly α line and deep X-ray data to identify active galactic nuclei (AGNs). In Section 2, we describe the rich ancillary data on the CDFS. In Section 3, we detail our data cube search methodology and use it to extract a sample of LAEs at $z \sim 1$. We also use simulations to estimate the completeness with which we can detect emitters of a given flux. In Section 4, we present the properties of the 28 new $z \sim 1$ LAEs that we found in our data cube search. We make use of the ancillary data to test the reliability of the LAEs and their UV redshifts and to get a first estimate of the AGN contamination. In Section 5, we present our discovery of a giant Ly α blob. We also compute the $z \sim 1$ LAE luminosity function, which we compare with LAE luminosity functions at lower and higher redshifts. In Section 6, we summarize our results.

We use a standard $H_0 = 70 \text{ km s}^{-1} \text{ Mpc}^{-1}$, $\Omega = 0.3$, $\Omega = 0.7$ cosmology throughout. All magnitudes are in the AB magnitude system.

2. CHOICE OF FIELD

The four deepest NUV grism observations (CDFS-00, 353 ks; GROTH-00, 291 ks; NGPDWS-00, 165 ks; COSMOS-00, 140 ks) correspond to some of the most intensively studied regions in the sky. In this paper, we use the central 50' by 50' region (centered on right ascension $3^{\text{h}}30^{\text{m}}40.2^{\text{s}}$ and declination $-27^{\circ}27'43.4''$ in J2000 coordinates) of the CDFS-00 for a pilot study to show the power of the data cube method. This region is extremely rich in ancillary information. For example, it contains the *HST* ACS Great Observatories Origins Deep Survey-South (GOODS-S; Giavalisco et al. 2004) subregion, where there are more than 3000 spectroscopic redshifts in a 140 arcmin^2 area (Le Fèvre et al. 2005; Mignoli et al. 2005; Vanzella et al. 2008; Popesso et al. 2009; Balestra et al. 2010; Cooper et al. 2012; Cowie et al. 2012). In Figure 1, we show how $> 80\%$ of the galaxies with $B < 24$ in the GOODS-S have spectroscopic identifications. In addition, multicolor observations from the *HST* programs GOODS-S (Giavalisco et al. 2004), Cosmic Assembly Near-Infrared Deep Extragalactic Legacy Survey (CANDELS; Grogin et al. 2011; Koekemoer et al. 2011), and Galaxy Evolution from Morphologies and SEDs (GEMS; Rix et al. 2004) provide the galaxy morphologies and spectral energy distributions from the rest-frame far-UV (FUV) to the mid-infrared for a substantial fraction of the objects. Finally, the 4 Ms *Chandra* image of the CDFS (Luo et al. 2008; Xue et al. 2011) and the Extended CDFS (ECDFS; Lehmer et al. 2005; Virani et al. 2006) fields can be used to help eliminate AGNs. A number of optical spectroscopic surveys have specifically targeted the X-ray sources in these fields (Szokoly et al. 2004; Treister et al. 2009; Silverman et al. 2010).

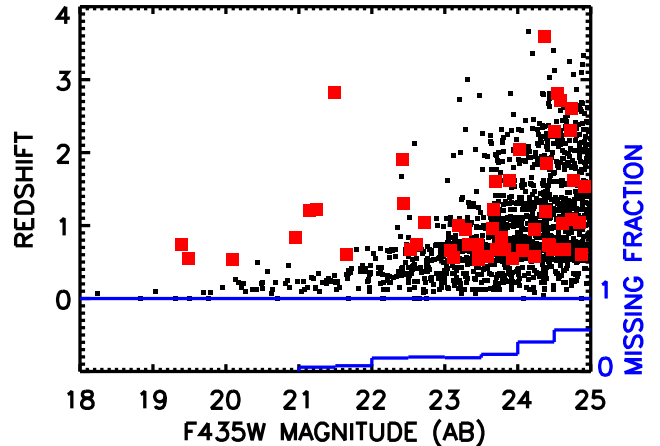


FIG. 1.— Spectroscopic redshift vs. F435W (B -band) magnitude for the sources in the GOODS-S (see references in text). The bottom blue histogram shows the fraction of sources without secure spectroscopic identifications. This fraction only becomes large fainter than $B = 24$. Red squares show sources classified as AGNs based on their X-ray luminosities (see Section 4).

3. METHODOLOGY

3.1. *GALEX* Spectral Images

The 50 cm *GALEX* telescope contains a selectable CaF₂ 75 g mm^{-1} grism, which provides slitless spectroscopy over the whole *GALEX* 1.25 deg diameter field-of-view. The grism is optimized for order 2 in the FUV channel ($1344 - 1786 \text{ \AA}$) and for order 1 in the NUV channel ($1771 - 2831 \text{ \AA}$). The resolution is roughly 10 \AA in the FUV ($R=200$) and 25 \AA in the NUV ($R=90$), though the exact resolution depends on both the wavelength and the spatial extent of the target (Morrissey et al. 2007).

The pipeline extractions of the *GALEX* grism data are described in Chapter 6 of the *GALEX* technical documentation and in the *GALEX* grism primer (<http://www.galex.caltech.edu/researcher/grism/primer.html>). The pipeline produces spectral images for each individual exposure, together with extracted one- and two-dimensional spectra from the combined exposures for all of the objects in the field down to a limiting NUV magnitude where the signal-to-noise of the continuum spectrum becomes low.

In the first stage of the *GALEX* grism reductions, the photons are processed in the same way as they are in the direct broadband images, and astrometrically corrected and registered whole field spectral images of the intensity and system response are created. These individual spectral images, with an average exposure time of about a thousand seconds, have been taken at a wide range of grism rotations. For the long total exposures of fields like the CDFS-00, there are several hundred such individual spectral images. We begin our own data reductions from these spectral images.

3.2. Data Cube Construction

The slitless nature of the grism data results in spectral overlaps between neighboring objects. However, because each of the spectral images is taken at a different rotation

angle, overlaps can be removed. Objects only overlap with a given neighbor at one orientation, and so in the multiple spectral images, the signal associated with a given object can be picked out from the occasional contamination. The grism data are often portrayed as a “propellor image”, where images at many grism angles are added together, as shown in Figure 2. This type of image is extremely useful for visualizing our present *GALEX* grism extraction process. Each pixel (x, y) on the spectral image corresponds to a specified position in right ascension and declination. At a given orientation, the grism spectrum corresponding to that pixel runs at that angle relative to the central position. The zeroth order lies to the negative side, while the higher orders lie to the positive side. Thus, for intensively observed fields with large numbers of independent spectral images, we can form a four-dimensional data cube (x by y by the number of wavelength elements by the number of spectral images). The number of x and y pixels corresponds to the total number of spatial pixels in the grism image (here 2000 by 2000), and we hereafter refer to the number of spectral images as NN.

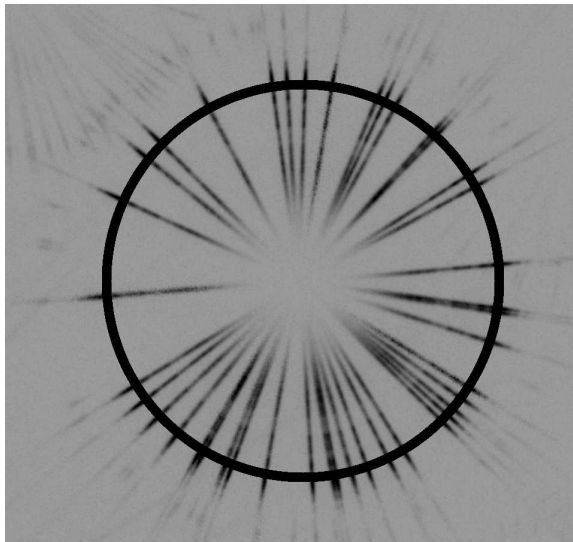


FIG. 2.— The well-known “propellor” image for a small subsample of spectral images in the CDFS-00. The image is the sum of a number of individual spectral images. We show only 40 of the 342 spectral images on the field. Each exposure is taken at a different angle. In a summed image such as this, they fan out in a propellor shape centered on the position of the galaxy (which is not seen in the grism spectra). For the NUV grism images shown here, the spectrum is dominated by the first order. For this order, a given wavelength corresponds to a circular annulus, such as that shown by the large circle. The flux at that wavelength may be obtained by forming a clipped average of the vector of fluxes in the region intercepted by the annulus and the spectra for the full image set (e.g., Keel et al. 2009).

A given wavelength corresponds to a circular annulus (large circle in Figure 2), the spokes of which correspond to the grism angles. A given emission line will occur at these specified positions in the suite of images with varying grism angles (e.g., Keel et al. 2009). If we construct a vector of values, only the object itself appears in all the elements. Other objects occur as random contamination in single elements of the vector. Thus, we can mask out pixels on the individual spectral images where we expect contamination from bright neighboring galaxies. We can further remove contamination from fainter objects by us-

ing a clipped average to determine the true signal. In doing so, we can collapse the four-dimensional data cube to a three-dimensional data cube (x by y by the number of wavelength elements). This final three-dimensional data cube is analogous to the data cube that would be obtained with a scanning imaging spectrometer or with an integral-field spectrograph where each spatial pixel has a spectrum associated with it. For most spatial pixels, there is no significant continuum flux or emission lines in the spectrum (the third axis). We may also view the three-dimensional data cube as a sequence of narrowband images, stepping in wavelength, each of which may be searched for emitters. It is in this way that we form our emission-line selected sample.

We created a pipeline to convert the NUV and FUV spectral images into four-dimensional data cubes. We chose a wavelength step of 5 Å for the NUV output cube in order to oversample the roughly 20 Å wavelength resolution. We chose the wavelength range (1930 – 2730 Å) to cover the 25% response range of the NUV grism. This gives 160 wavelength elements.

In forming the four-dimensional data cubes (x by y by 160 by NN), we wanted to maintain the statistical independence of the pixels. Thus, in assigning to each (x, y, λ) a vector (the fourth axis), we need to be concerned with the fact that we are oversampling the spectral images in wavelength. To avoid averaging, we decided to assign to each (x, y, λ) position in a given spectral image (recall that each position will have NN values since there are NN spectral images) the nearest neighbor pixel using the grism angle from the *GALEX* pipeline. Note that the *GALEX* pipeline computes the grism angle by fitting to the spectra of bright objects in the field. To maintain the statistical independence of the pixels, we will only assign each pixel in a given spectral image once, so since we are oversampling the spectral images in wavelength, this means that some of the pixels in the fourth axis are blank. These blank pixels are ignored hereafter.

At this point, we collapsed the fourth axis by forming the median, comparing each value in the fourth axis with the median, and eliminating points that deviate from the median by more than 5σ . We formed an exposure time-weighted average from the remaining points to give the final signal at this (x, y, λ) pixel in the three-dimensional data cube.

We used an identical procedure for the FUV processing, except here we chose a wavelength step of 2.5 Å over the wavelength range 1345 – 1745 Å, giving 160 wavelength elements. Also, because of the low background photon detection rate per pixel in the FUV, and because contamination is much less of a problem in the FUV, we formed a simple average rather than a median for comparison with each value in the fourth axis. We eliminated points that deviated from the average by more than 5σ . Then, as we did for the NUV processing, we formed an exposure time-weighted average of the clipped vector to obtain the final signal at this (x, y, λ) pixel in the three-dimensional data cube.

For the present emission-line search, we are not interested in the objects with brighter continua whose spectra are already included in the existing *GALEX* pipeline data products. We also want to minimize any contamination from these brighter galaxies and stars in the final

three-dimensional data cube. We therefore masked out the spectral region in each *GALEX* spectral image that corresponded to a pixel with a surface brightness in excess of $25.8 \text{ mag arcsec}^{-2}$ in the NUV continuum image of the field smoothed with a 2 pixel boxcar smoothing. This removes all objects with NUV magnitudes brighter than 20.4 and no objects with NUV magnitudes fainter than 21.25. This faint magnitude bound is considerably brighter than the magnitude limit of the pipeline sample, so we only eliminate objects that already have spectra and hence already have been searched for Ly α lines. (The remaining objects that are already present in the pipeline sample are eliminated later in the process; see Section 3.3.) None of our results are sensitive to the precise choice of the masking surface brightness threshold.

In Figure 3 (left panel), we show a typical portion of a wavelength “slice” (a 40 \AA region obtained by summing eight of the 5 \AA steps; see Section 3.3) in the final data cube compared to (right panel) the corresponding NUV continuum image. The positions in the final data cube that correspond to the regions that were masked appear white in the wavelength slice image. 10901 spatial pixels are eliminated by the masking, or just under 0.3% of the spatial area covered by the three-dimensional data cube.

3.3. Data Cube Search

With the three-dimensional data cube in hand, we can now carry out a search for emission-line objects. We first divided each 5 \AA wavelength slice in the data cube by the grism effective area at that wavelength to take out response variations. We used the values given in <http://galexgi.gsfc.nasa.gov/docs/galex/Documents>. We then formed forty 20 \AA (in order to roughly match the resolution element) narrowband slices from the NUV data cube. For each slice, we subtracted the average of slices on either side of the primary slice, N. We used slices N-5 to N-3 and slices N+3 to N+5 to form this average. The background subtraction removes most of the residual structure and most of the continuum objects in the field, as we see by comparing the left panel of Figure 3 with the upper-right panel of Figure 4. This will retain any emitter whose width is less than about 240 \AA . Even broad-line AGNs satisfy this criterion, so we should not be eliminating any objects by this process.

From the left panel of Figure 3, we can see residual regions around the small number of very bright sources that were masked, and these can cause contamination. Thus, in each of the 40 slices, we masked out additional spatial regions around these bright sources. For sources with NUV magnitudes brighter than 14, we masked a $4'$ radius region around the source, and for sources with NUV magnitudes brighter than 17, we masked a $1.5'$ radius region.

We searched each slice for objects with surface brightnesses of at least $2 \times 10^{-6} \text{ photons cm}^{-2} \text{ s}^{-1}$ per $1.5''$ spatial pixel using a 4 pixel spatially smoothed version of the slice. The smoothing roughly matches the $5.3''$ spatial resolution in the *GALEX* NUV band. The surface brightness cut was chosen empirically to provide the maximum depth while not generating an unmanageably large number of spurious sources that have to be eliminated by hand. Bright emitters may appear in more than one slice, and we formed our preliminary catalog by merging all of

the emitters found in neighboring slices. As a consequence of the background subtraction process, we only cover a wavelength range of 2030 to 2630 \AA , which corresponds to a redshift range for Ly α of $z = 0.67 - 1.16$. At this stage, any objects already in the pipeline sample were removed.

We created the one-dimensional spectra directly from the three-dimensional data cube using a 4×4 spatial pixel box together with a local background subtraction. We flux calibrated by matching to the NUV magnitude of the object. We visually inspected each of the narrowband slices and the one-dimensional spectrum of each selected object and eliminated objects that were artifacts, such as remaining edge effects from the brighter objects or objects with stellar spectra, to form our primary catalog. The initial selection yielded 161 objects, of which we retained 28.

For each of the 28 objects, we also created a two-dimensional spectral image from which we could extract final one-dimensional spectra. For doing the extractions, we created our own version of the *GALEX* pipeline. The only difference between our version of the pipeline and the standard pipeline is that we used a profile-weighted spectral extraction to form the one-dimensional spectra (Horne 1986). As we illustrate in Figure 5, we obtained some slight improvements in signal-to-noise from the profile weighting (about a factor of 1.3), which is helpful in dealing with weak features, such as the faint Ly α emission lines. (Note that the source shown in Figure 5 was from the pipeline sample rather than from our data cube sample.)

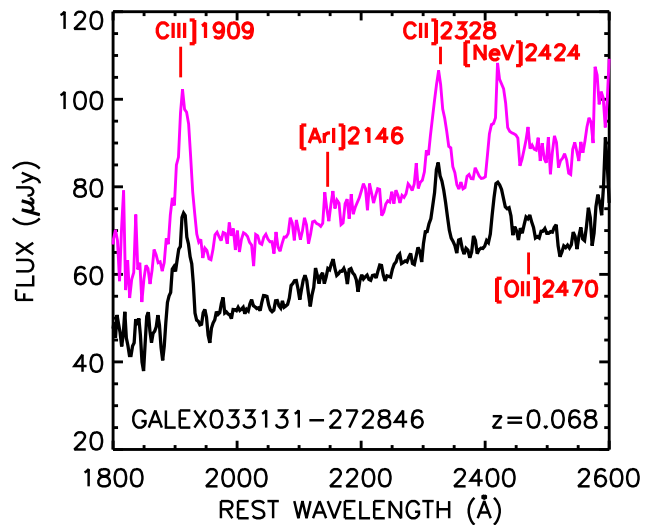


FIG. 5.— Spectrum of a low-redshift narrow-line Seyfert found in the CDFS-00 field. We show only the portion of the spectrum covered by the NUV spectrum. The purple spectrum shows the *GALEX* pipeline extraction, while the black spectrum shows our version, which does a profile-weighted extraction (displaced downwards in normalization for comparison purposes). The optimal weighting in our extraction provides a slight gain (about 30%) in signal-to-noise, which allows us to see the weak [OII] λ 2470 line. The [ArI] λ 2146 line is still too weak to be seen.

In Figure 6, we show the two-dimensional NUV spectral images of our 28 new $z \sim 1$ LAEs, ordered according to Table 1 (see Section 4), along with their FUV and NUV continuum images (shown to the far-left and left of each spectral image, respectively). In Figure 7, we show the one-dimensional spectra that we extracted from these. We performed the final flux calibration using the given *GALEX* spectral response.

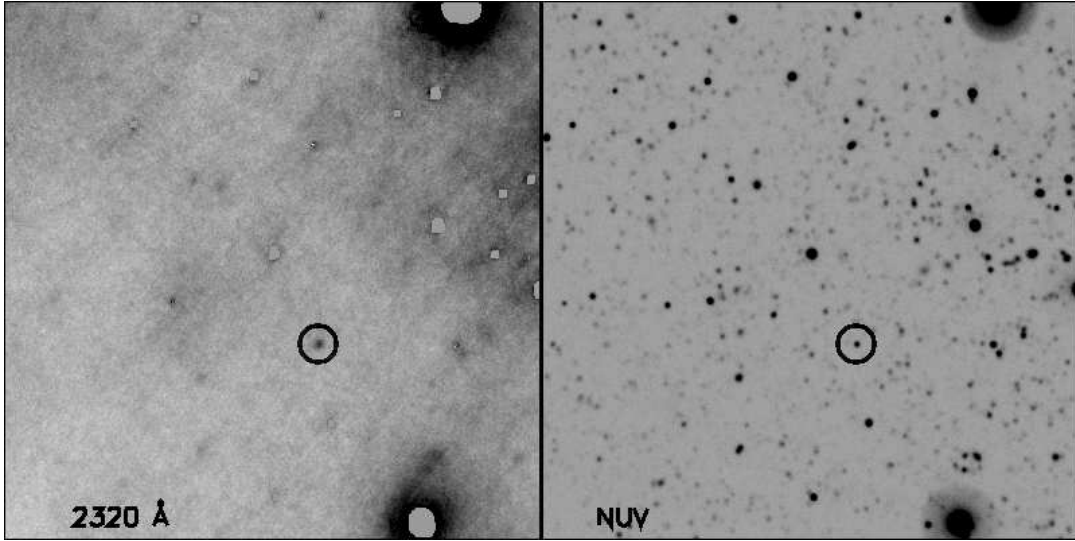


FIG. 3.— (Left) A 40 \AA image slice (centered at 2320 \AA) of the CDFS-00 NUV data cube. The spatial area is $10'$ by $10'$, centered at a right ascension of $3^{\text{h}}32^{\text{m}}10.18^{\text{s}}$ and a declination of $-28^{\circ}12'46''.1$. Brighter galaxies in the field have been zeroed out in this data cube extraction, as described in the text, though there are still residuals around the edges of these masked regions that can cause contamination. We mask these regions at a later stage. The variation in the background is caused by the relative positions of bright stars in the field. The circled object is an emitter, GALEX033202-281408, which we use to illustrate our search procedure in Figure 4. (Right) Corresponding NUV continuum image with the emitter circled.

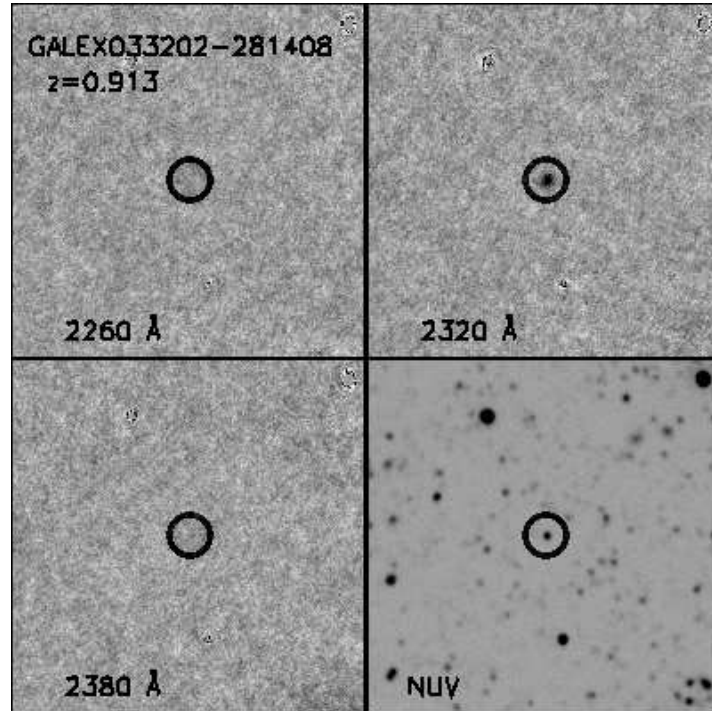


FIG. 4.— Three $5' \times 5'$ background subtracted 20 \AA image slices and the corresponding NUV continuum image to illustrate the search procedure for finding LAEs in the CDFS-00 NUV data cube. The images correspond to a portion of the region shown in Figure 3 and are centered on the detected LAE GALEX033202-281408, which is circled. This LAE has a flux of $3.1 \times 10^{-15} \text{ erg cm}^{-2} \text{ s}^{-1}$ and a UV spectral redshift of $z = 0.913$. It appears in the image slice at 2320 \AA but not in the off emission-line slices at 2260 \AA and 2380 \AA . It corresponds to a relatively bright object (21.9 mag) in the NUV continuum image and only just misses being included in the *GALEX* pipeline sample.

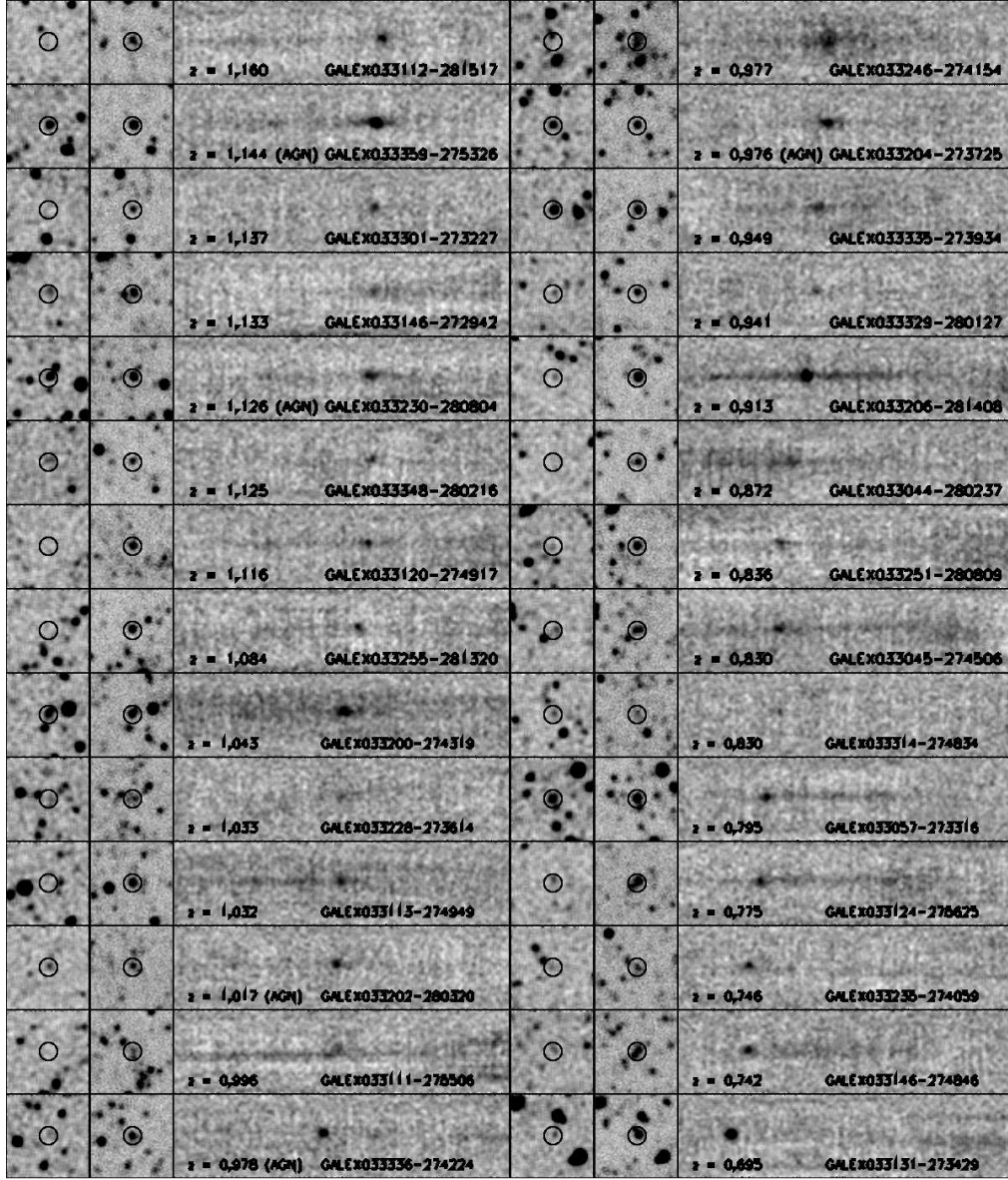


FIG. 6.— Two-dimensional spectral images of the 28 new $z \sim 1$ LAEs found in our CDFS-00 NUV data cube search, ordered by decreasing redshift, as in Table 1. The x-axis corresponds to the wavelength range 1892 – 3119 Å, and the y-axis corresponds to the spatial dimension. The spectral images are labeled with the UV spectral redshift; with “AGN”, if the source were classified as an AGN based on the presence of high-excitation lines in the UV spectrum; and with the *GALEX* name. The two small panels at the far-left and left of each spectral image are broadband FUV and NUV images, respectively, with the position of the emitter circled in each. The Ly α blob is the upper-right corner spectrum.

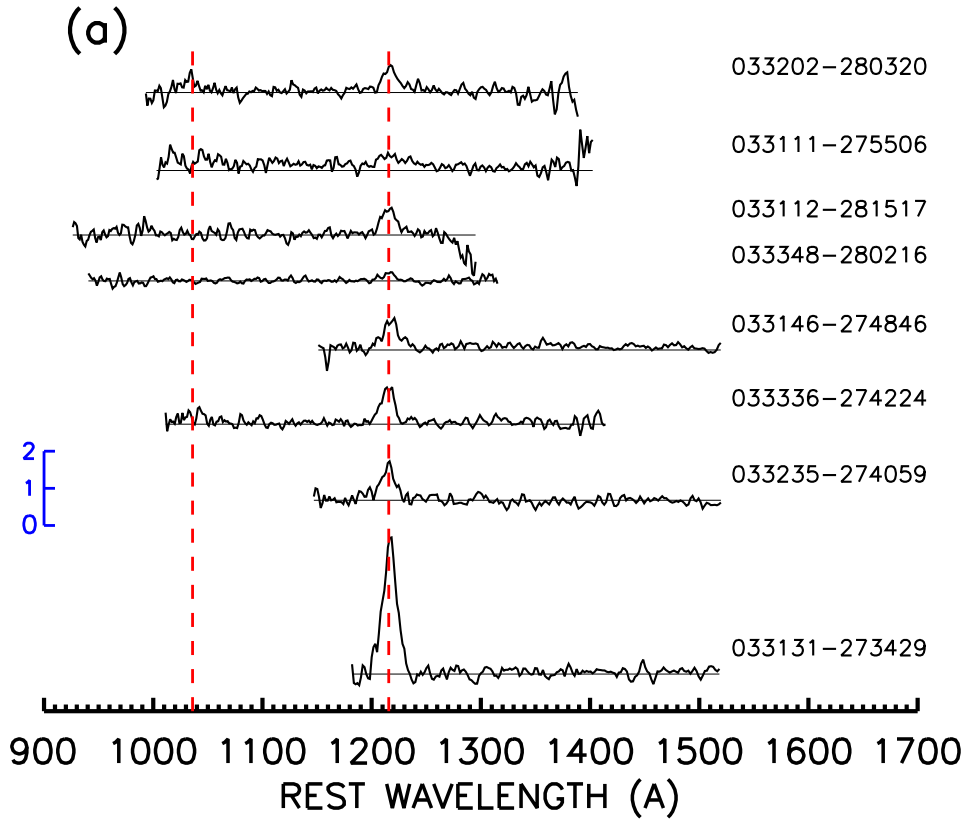


FIG. 7.— (a-d) One-dimensional spectra of the 28 new $z \sim 1$ LAEs found in our CDFS-00 NUV data cube search, ordered by decreasing redshift, as in Table 1. The spectra are plotted against rest wavelength and are in units of $10^{-16} \text{ erg cm}^{-2} \text{ s}^{-1} \text{ \AA}^{-1}$, with the scale shown at the left side of each panel. The red dashed lines show the positions of Ly α and OVI 1036.

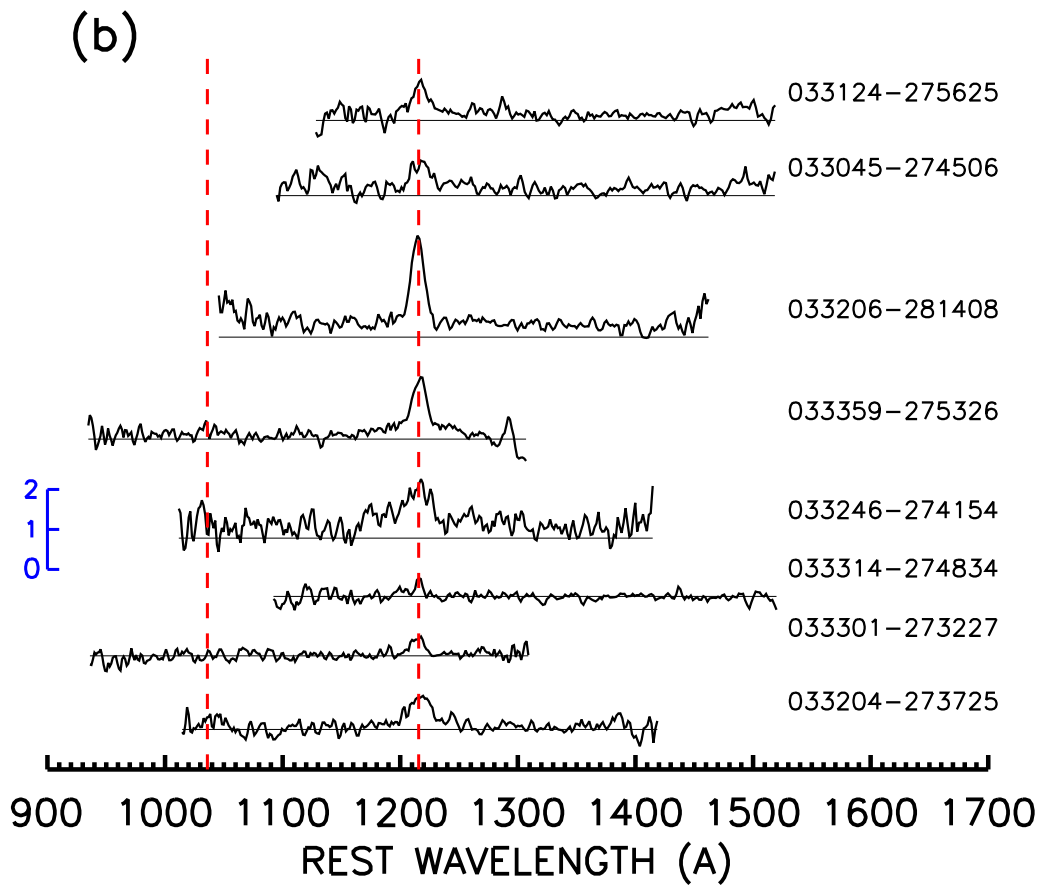


FIG. 7.— (b)

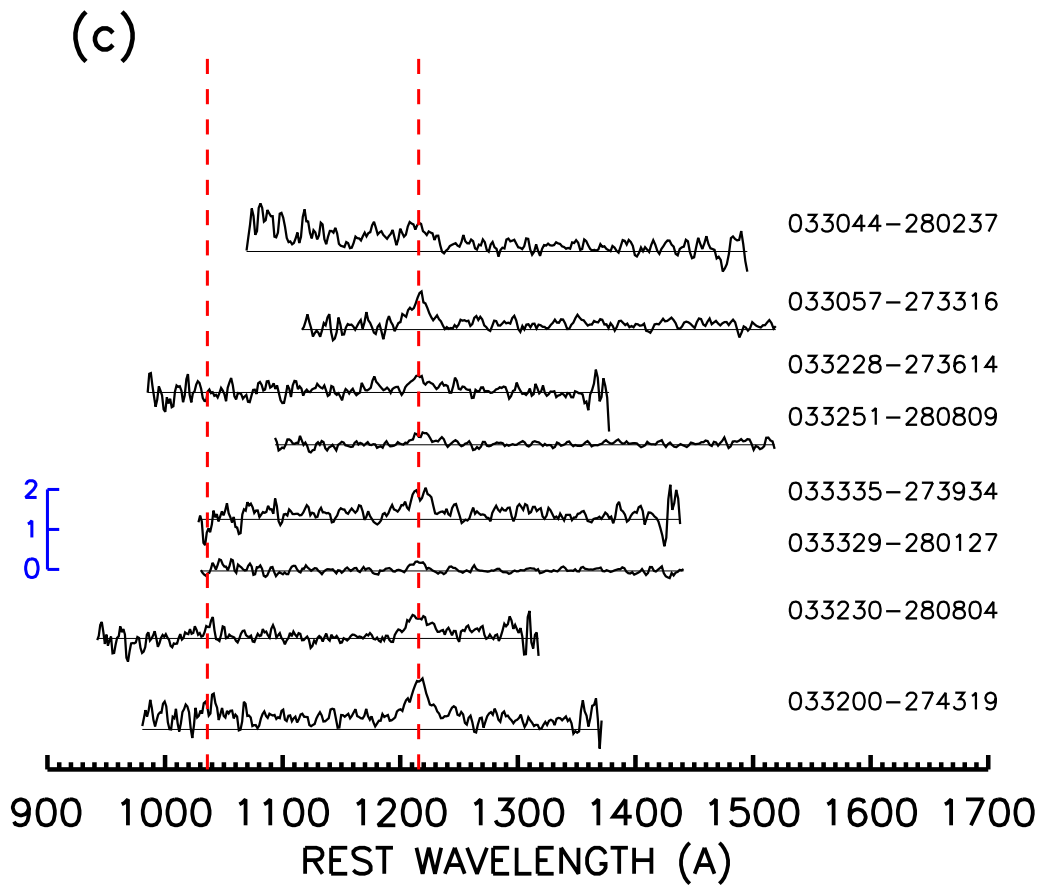


FIG. 7.— (c)

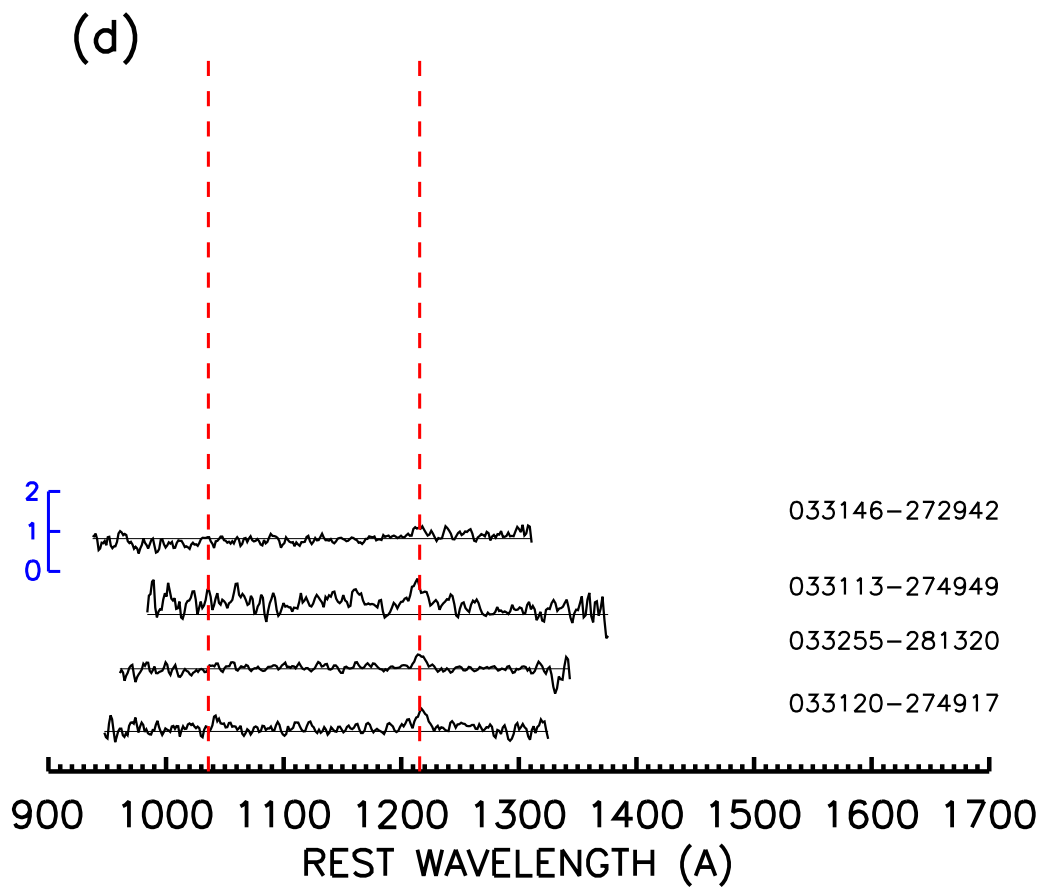


FIG. 7.— (d)

We decided that using the one-dimensional spectra formed from our version of the pipeline software rather than the one-dimensional spectra obtained from the data cube would enable us to make the most direct comparison with brighter emitters in the field, since their spectra had been formed from the pipeline software. As a bonus, it would also provide an independent confirmation of the emission-line selection. In Figure 8, we compare the one-dimensional spectra formed in the two different ways using two of the emitters. Despite the very different procedures used, the two methods produce spectra that agree well in shape and normalization.

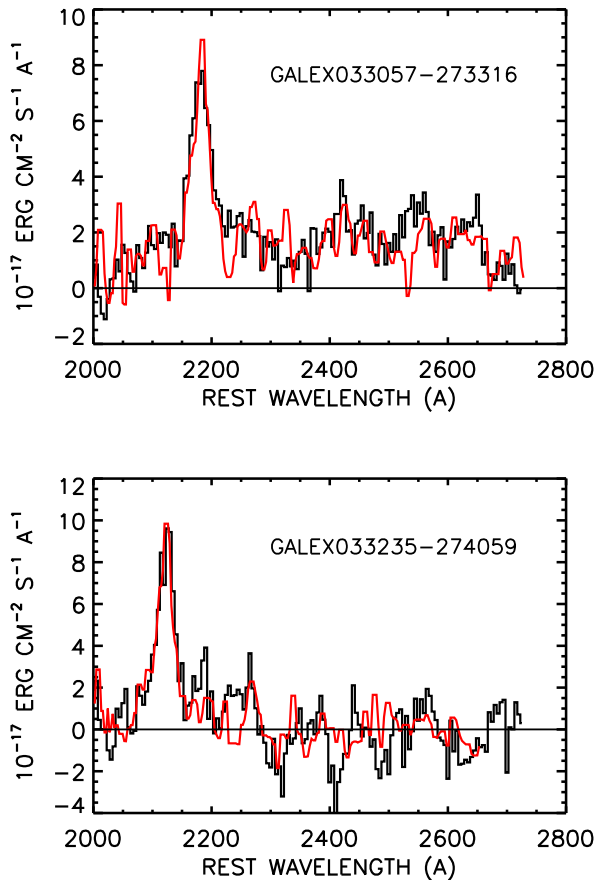


FIG. 8.— Comparison of the spectra of two emitters in the CDFS-00 obtained in two ways: from our three-dimensional NUV data cube (black) and from our version of the *GALEX* pipeline (red). For each emitter, the name is given in the upper right of the panel. As discussed in the text, the extraction methods and the absolute flux calibration differ for the data cube spectra and the pipeline spectra, so the agreement provides a test of the two methods.

For each of the 28 objects, we checked that the discovered line was not clearly another line rather than $\text{Ly}\alpha$ by using the combined FUV and NUV spectra. For the spectrum shown in Figure 5, the discovered line was not $\text{Ly}\alpha$, but as we noted above, this object was from the pipeline sample rather than from our data cube sample. All of the lines in our data cube sample appear to be $\text{Ly}\alpha$.

We measured the redshifts, the $\text{Ly}\alpha$ fluxes, and the line widths by fitting a Gaussian to the primary line in each spectrum. Since, in general, the continua are faint in the spectra, we obtained the EWs of the lines by dividing the measured $\text{Ly}\alpha$ flux by the continuum flux measured from

the broadband NUV continuum image. We also made a classification of whether the emitter was definitely an AGN based on the presence of high-excitation emission lines in its UV spectrum, or whether it could be a star-forming galaxy (see, e.g., Cowie et al. 2010). Our candidate star-forming galaxy sample will still contain some remaining AGNs, so optical spectra and/or X-ray imaging data are needed to make a final determination of whether a galaxy is, in fact, star-forming.

3.4. Completeness of Recovery Versus Flux

Because of the low spatial and spectral resolution of the *GALEX* grism data, the emitters almost all appear as unresolved objects in the narrowband slices or in the two-dimensional spectral images (Figure 6). The one exception to this is GALEX033246-274154, which is clearly extended. In Figure 9a, we show a contoured image (black) of a typical emitter, and in Figure 9b, we show a similar image for GALEX033246-274154. In both panels, we also show the point spread function contours formed from the average of the three brightest sources in the sample (red). There is a clear distinction between the two panels. In order to be spatially resolved, the object must be very extended. Thus, we shall interpret GALEX033246-274154 as a $\text{Ly}\alpha$ blob in the discussion section.

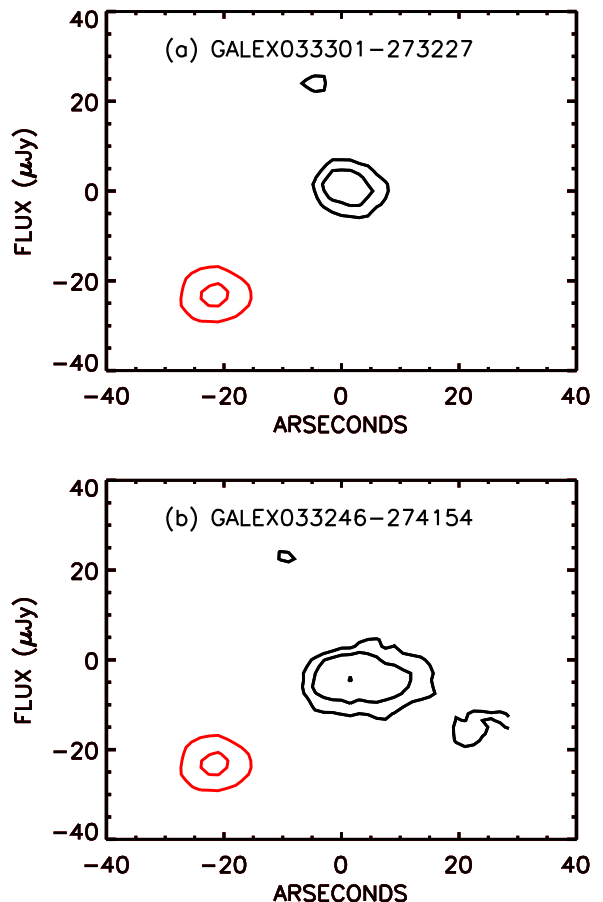


FIG. 9.— Narrowband contoured images (black) of (a) a typical emitter, which is spatially unresolved, and (b) the $\text{Ly}\alpha$ blob. The red contours show the point spread function formed from the average of the three brightest sources in the sample.

Since nearly all the emitters in our sample are unresolved, it is relatively straightforward to estimate the com-

pleteness with which we can detect emitters of a given flux, since we do not need to consider morphological or size differences. In addition, since the observed-frame equivalent widths of the objects are large compared to the spectral resolution, the emission-line peaks have a high contrast with the continuum level (Figure 7). Thus, the selection depends only on the emission-line flux and not on the continuum level, or, as a corollary, on the equivalent width.

In order to estimate the completeness, we added in 3000 objects (one hundred emitters in each of the thirty narrow-band slices) of a specified flux with shapes corresponding to the spatial point spread function measured using bright objects in the data cube. The emitters were added into the data cube at random spatial positions and uniformly distributed through the narrowband slices. We then ran our standard selection procedure and found the number of recovered objects. At fluxes above 10^{-15} erg cm $^{-2}$ s $^{-1}$, our selection is more than 80% complete, but it drops extremely rapidly below this value (see Figure 10). We shall use this in calculating the Ly α luminosity function.

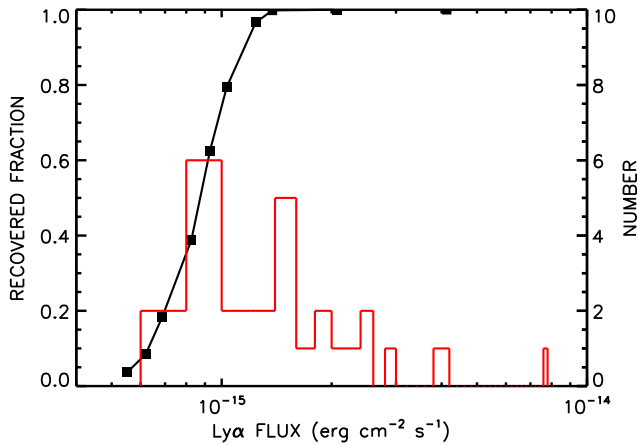


FIG. 10.— Fraction of simulated sources recovered as a function of the emission-line flux (black curve with squares at the measured fluxes). The red histogram shows the number of detected sources as a function of flux in 2×10^{-16} erg cm $^{-2}$ s $^{-1}$ bins. The counts flatten out and drop at low fluxes where the incompleteness becomes important.

4. NEW Ly α EMITTERS IN THE CDFS

In Table 1, we summarize the properties of the 28 new $z \sim 1$ LAEs in the CDFS-00 found in our data cube search. These are all objects that were not present in the pipeline sample. In Column 1, we give the *GALEX* name; in Columns 2 and 3, the J2000 right ascension and declination; in Columns 4 and 5, the NUV and FUV AB magnitudes; in Column 6, the redshift from the *GALEX* UV spectrum; in Column 7, the Ly α fluxes with 1σ errors; in Column 8, the logarithm of the Ly α luminosity; in Column 9, the rest-frame EW(Ly α) with 1σ errors; in Column 10, an entry of “AGN”, if the source is classified as an AGN based on its UV spectrum; in Column 11, the logarithm of the 2–8 keV flux, if the source is detected in the Extended CDFS, or an entry of “ECDFS”, if the source is in the ECDFS region but is not detected; in Column 12, the optical ground-based redshift; and in Column 13, the optical spectral classification.

We measured the NUV and FUV AB magnitudes in $8''$ diameter apertures centered on the emitter positions. We corrected these to total magnitudes by measuring for the brighter objects (20–23 mag range) the offset between the aperture magnitudes and the magnitudes of the pipeline sample. The 1σ errors obtained by measuring magnitudes at random positions in the images are 26.0 for the NUV and 26.7 for the FUV. All of the objects are bright in the NUV, but some are not detected in the FUV. For objects where we measure a negative flux in the FUV, the quantity in Column 5 is the magnitude corresponding to the absolute value of the flux with a minus sign in front to indicate that the flux was negative.

When allowance is made for the masking done on bright sources (see Sections 3.2 and 3.3), the area covered is 2286 arcmin 2 , and the data cube emission-line search procedure covers a redshift range for Ly α detections of $z = 0.67–1.16$. The observed comoving volume is 2.3×10^6 Mpc 3 .

Thirteen of the LAEs lie in the area covered by the deep X-ray exposures of the ECDFS (Lehmer et al. 2005; Virani et al. 2006); six of these thirteen LAEs are detected in X-rays (see Column 11). At $z \sim 1$, the ECDFS sensitivity limit ($f_{2-8 \text{ keV}} \sim 6.7 \times 10^{-16}$ erg cm $^{-2}$ s $^{-1}$) is close to the X-ray luminosity threshold of 10^{42} erg s $^{-1}$ that is usually used to define AGN activity (e.g., Hornschemeier et al. 2001; Barger et al. 2002; Szokoly et al. 2004; Silverman et al. 2005), so the sources that are not detected have X-ray luminosities consistent with being star-forming galaxies. We hereafter refer to the sources that are X-ray detected (and hence are clearly AGNs based on their X-ray luminosities) as X-ray AGNs.

Nine of the LAEs have optical spectroscopic redshifts (see Column 12). For all of these sources, the optical redshift confirms the UV redshift derived from the data cube search. Four of these nine are X-ray AGNs, which is not too surprising, given that the spectroscopy in the ECDFS region was concentrated on X-ray selected objects. The mean offset and dispersion between the ground-based optical and the *GALEX* UV redshifts is $z_{\text{ground}} - z_{\text{galex}} = -0.004 \pm 0.003$.

All three of the sources in the ECDFS region that were classified as AGNs based on the presence of high-excitation lines in their UV spectra are also X-ray AGNs. In the other direction, three of the 6 sources classified as X-ray AGNs were already classified as AGNs based on their UV spectra. Of the remaining three sources, GALEX033131-273429 is classified as a Seyfert 2 (Sy2) based on the presence of [NeV] λ 3426 in its optical spectrum, and, as can be seen in Figure 7a, has a single narrow but very strong Ly α emission line in the UV but no obvious CIV λ 1549 emission; GALEX033202-274319 is classified as a broad-line AGN from its optical spectrum; and GALEX033335-273934 has not been optically observed. In the case of the latter two objects, their redshifts are poorly positioned to detect either OVI λ 1036 or CIV λ 1549 in their UV spectra, and only their Ly α lines are seen.

Classifying sources as AGNs based on their UV spectra can be challenging, since quite often CIV is not accessible, and, as can be seen from Figure 7, OVI is typically quite weak. The fraction of LAEs in the ECDFS region that were not classified as AGNs based on their UV spectra (10 sources) but are classified as AGNs based on their op-

tical spectra (2 sources) is 20%. This is very similar to the $\sim 20\%$ found for the LAEs in the *GALEX* pipeline samples (Finkelstein et al. 2009b; Scarlata et al. 2009; Cowie et al. 2010; see Cowie et al. 2011 for a discussion of the variations in the measurements of this quantity).

We conclude that the bulk of the LAEs found in our data cube search are real and that the UV spectroscopic redshifts based on the Ly α identifications are reliable.

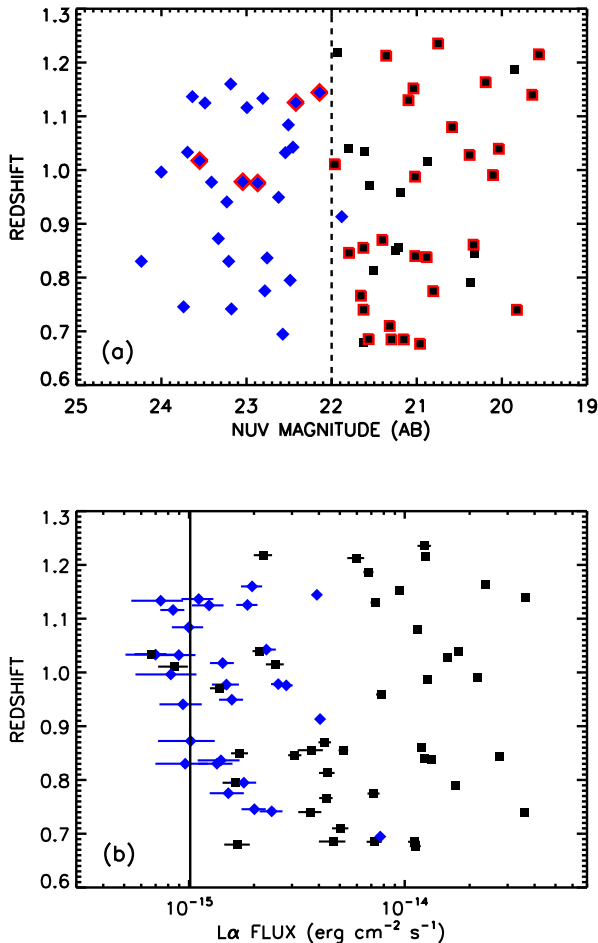


FIG. 11.— (a) *GALEX* redshift vs. NUV magnitude. Black squares show the CDFS-00 LAEs found by Cowie et al. (2010, 2011) in the *GALEX* pipeline sample of $\text{NUV} < 22$ (dashed line) continuum-selected objects in the CDFS-00 field. Blue diamonds show the new CDFS-00 LAEs found in our data cube search; none of these were in Cowie et al. Note that the redshift range searched in the data cube is slightly smaller. Objects with high-excitation UV lines (we classified these sources as AGNs based on their UV spectra) are surrounded by larger red symbols. (b) *GALEX* redshift vs. Ly α flux. The symbols are as in (a). We show 1σ error bars on the Ly α fluxes. Solid line shows the Ly α flux above which more than 80% of the emitters are detected (see Fig. 10).

5. DISCUSSION

We now consider how the properties of the CDFS-00 LAEs in our data cube sample compare with those of the CDFS-00 LAEs in the pipeline sample. In Figure 11a, we illustrate how, by construction, the pipeline misses sources fainter than the pipeline magnitude limit of $\text{NUV} \sim 22$ (dashed line). We show the *GALEX* redshifts versus the NUV magnitudes for the CDFS-00 LAEs found by Cowie et al. (2010, 2011) (black squares) and the new CDFS-

00 LAEs found by our NUV data cube search (blue diamonds). In contrast, in Figure 11b (symbols and colors as in Figure 11a), we show how there is substantial overlap in the Ly α emission-line fluxes of the two samples, since this quantity depends on both the NUV magnitude and the $\text{EW}(\text{Ly}\alpha)$. Here we can see that the pipeline extraction begins to miss sources below a Ly α flux of about $8 \times 10^{-15} \text{ erg cm}^{-2} \text{ s}^{-1}$ and becomes progressively more incomplete at fainter fluxes, until below $2 \times 10^{-15} \text{ erg cm}^{-2} \text{ s}^{-1}$, very few sources are detected in the pipeline extraction.

In Figure 11a, we use larger red symbols to denote sources with high-excitation UV lines (in addition to Ly α) in their *GALEX* spectra. These sources are classified as AGNs based on their UV spectra. We can see that at $\text{NUV} < 22$, most of the sources are AGNs. Thus, the only way to probe the bulk of the LAE galaxy population at these redshifts is to do a data cube search of the present type.

The sources found in the data cube search and missed in the pipeline are those with high EWs. The progressive increase in incompleteness with decreasing Ly α flux can be illustrated by the number of sources lying above the EW threshold at a given Ly α flux. We show this in Figure 12 (symbols and colors as in Figure 11), where we plot rest-frame EW versus Ly α flux. For a given Ly α flux and redshift, the $\text{NUV} = 22$ continuum cut corresponds to a given EW. We show these cuts in the figure at the upper (dashed diagonal) and lower (solid diagonal) end of the $z = 0.67 - 1.16$ redshift range. They become progressively lower as we move to fainter Ly α fluxes, such that fewer of the emitters are included in the pipeline sample.

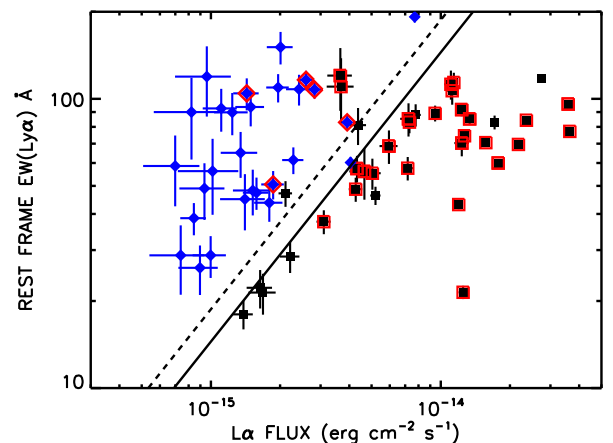


FIG. 12.— Rest-frame $\text{EW}(\text{Ly}\alpha)$ vs. Ly α flux. Black squares show the CDFS-00 LAEs found by Cowie et al. (2010, 2011) in the *GALEX* pipeline sample of $\text{NUV} < 22$ continuum-selected objects in the CDFS-00 field. Blue diamonds show the new CDFS-00 LAEs found in our data cube search; none of these were in Cowie et al. Objects with high-excitation UV lines (we classified these sources as AGNs based on their UV spectra) are surrounded by larger red symbols. We show 1σ error bars on the Ly α fluxes and equivalent widths. The *GALEX* pipeline sample only has sources with EWs below the value set by the NUV magnitude limit (diagonal lines illustrate the effects of the redshift range: $z = 0.67$ —solid; $z = 1.16$ —dashed). The black squares should lie below these lines, and the blue diamonds should lie above these lines. Clearly, as one moves to lower Ly α fluxes, the continuum-selected pipeline extraction starts to miss most of the LAEs.

We next inspected the UV/optical images of the full CDFS-00 LAE sample (i.e., this includes both the pipeline and the data cube LAE samples) in the redshift range $z = 0.67 - 1.12$. All but one of these LAEs are covered by deep U -band imaging data obtained with the wide-field (1 deg^2 field-of-view) imaging camera MegaPrime/MegaCam on the 3.6 m Canada-France-Hawaii Telescope (CFHT). The Canadian Astronomy Data Centre (CADC) reduced the data using the MegaCam Image Stacking Pipeline (MegaPipe; Gwyn 2008) and give the 5σ AB magnitude limits as ranging from 26.5 to 27.0. Only one of the observed objects (GALEX033246-274154) does not have a clear counterpart in the CFHT U -band.

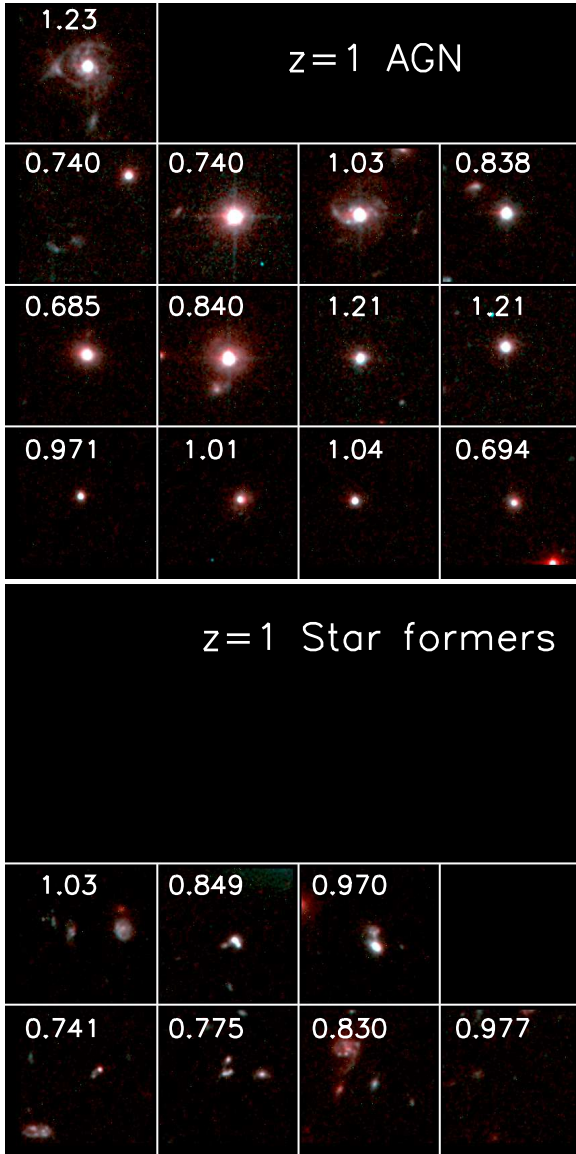


FIG. 13.— Images from the GEMS survey (Rix et al. 2004) of LAEs found either in the CDFS-00 *GALEX* pipeline sample or in our data cube search. The lower 7 sources are candidate star-forming galaxies in the region, and the top 13 sources are AGNs based on either their UV continuum lines or their X-ray luminosities. Each thumbnail is $6''$ on a side. The blue and green colors correspond to the F606W GEMS image, and the red color corresponds to the F850W GEMS image.

In addition, 20 of the 70 LAEs in the full CDFS-00 sample are in the GEMS region (Rix et al. 2004), where high

spatial resolution *HST* images are available. We show the GEMS images in Figure 13. We have divided these into two groups: AGNs (based on either their UV spectral signatures or their X-ray luminosities, which turns out to include all of the objects that were classified as AGNs based on their optical spectra) and star-forming galaxies (no high-excitation UV lines and not detected in X-rays). It appears that the morphologies of the objects follow their classifications: the AGNs are dominated by compact nuclei, while the star-forming galaxies are primarily resolved small blue galaxies, often with multiple components.

In addition to not being detected in the CFHT U -band, GALEX033246-274154 (last thumbnail of the bottom row in Figure 13) is not clearly detected in the *HST* images. GALEX033246-274154 appears to be a rather unusual object. It is clearly visible both in the NUV continuum image and in the UV spectral image (Figure 6) and hence is real. Furthermore, it is spatially resolved (Figure 9b). Its major axis is $18''$ and its minor axis is about $9''$, giving a linear major-axis diameter of 120 kpc and placing it in the category of the giant $\text{Ly}\alpha$ blobs, though its $\text{Ly}\alpha$ luminosity is at the low end of these objects (Matsuda et al. 2011).

Fortunately, a much deeper U -band image than the CFHT MegaPrime image was taken (Nonino et al. 2009) with the VIMOS instrument on the ESO VLT and covers the central region of the field, including this object. In Figure 14, we compare the FUV image (1st thumbnail) of the source (located at the center of each image) and the NUV image (2nd thumbnail) with the VIMOS U -band image (3rd thumbnail) and a K_s -band image (final thumbnail). In Figure 15, we overlay the contours of the emission-line region on the VIMOS U -band image. From these images, we see that the emission-line region corresponds to a faint diffuse U -band continuum structure. The object appears very similar to higher redshift $\text{Ly}\alpha$ blobs (e.g., Prescott et al. 2012).

We have marked the nearest X-ray selected AGN (circle) on the final thumbnail in Figure 14. It lies at about $14''$ from the blob. However, this AGN has a redshift of $z = 0.740$ and hence cannot be the excitation source for the blob. A more probable candidate (square) is an AGN that lies $25''$ (170 kpc) from the blob. Its redshift of $z = 0.982$ roughly matches that of the blob ($z = 0.977$).

Matsuda et al. (2011) found 10 giant $\text{Ly}\alpha$ blobs at $z = 3.1$ in a comoving volume that is almost identical to the present one. This suggests that the comoving volume density of giant blobs has dropped by almost an order of magnitude between $z = 3$ and $z = 1$ (see also Keel et al. 2009). However, a larger sample and a fuller understanding of the selection effects in the two samples would be needed to refine this result. We postpone a detailed analysis to a future paper (I. Wold et al. 2012, in preparation), where we plan to conduct data cube searches of all of the deep *GALEX* grism fields.

Finally, we computed the $\text{Ly}\alpha$ luminosity function of the CDFS-00 LAE galaxy sample in the redshift range $z = 0.67 - 1.16$ using the $1/V$ technique (Felten 1976), calculating the accessible volumes from the area of the sample. We used a flux limit of $7 \times 10^{-16} \text{ erg cm}^{-2} \text{ s}^{-1}$ and only included sources that were not classified as AGNs in any way and that have rest-frame $\text{EW}(\text{Ly}\alpha) \geq 20 \text{ \AA}$. (Note that the $\text{EW}(\text{Ly}\alpha) \geq 20 \text{ \AA}$ criterion is what is normally

used to define the high-redshift LAE population; e.g., Hu et al. 1998.) With these criteria, the sample includes two CDFS-00 LAE galaxies from the pipeline sample of Cowie et al. (2011; their Table 2), and the rest come from our data cube sample. We show the Ly α luminosity function (black squares) in Figure 16, along with the Ly α luminosity functions at $z = 0.3$ (blue dotted curve) and $z = 3.1$ (red solid curve) using the Schechter (1976) function fits given in Cowie et al. (2010) and Gronwall et al. (2007), respectively. The open squares show the computation when we do not correct for the effects of incompleteness, and the solid squares when we do using the results from the simulations (Figure 10). The dynamic range in luminosity is not large enough to justify fitting a Schechter function, but as we illustrate with the red dashed curve, the data can be well described by the Gronwall et al. (2007) luminosity function with the normalization (ϕ_*) reduced by a factor of 30.

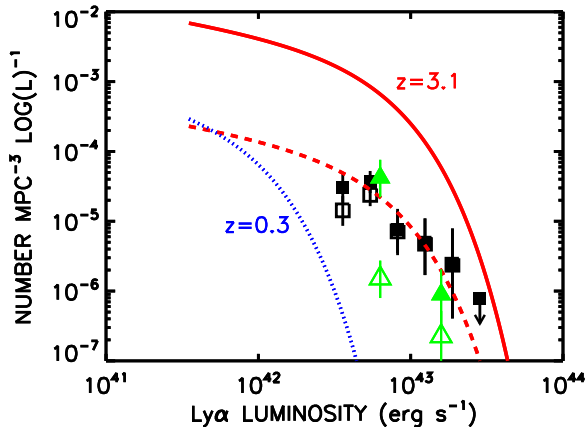


FIG. 16.— Derived Ly α luminosity function at $z = 0.67 - 1.16$ for the LAE galaxies in the CDFS-00 with $\text{EW}(\text{Ly}\alpha) \geq 20 \text{ \AA}$ from both the *GALEX* pipeline and data cube samples (black squares: open—raw data; solid—corrected for the effects of incompleteness using the results from the simulations; see Figure 10). Error bars are $\pm 1\sigma$ from the Poisson errors corresponding to the number of sources in the bin. Green open triangles show the luminosity function at $z = 0.65 - 1.25$ calculated by Cowie et al. (2011) for their 5 $\text{NUV} < 22$ pipeline extracted, optically confirmed, star-forming LAEs with rest-frame $\text{EW}(\text{Ly}\alpha) \geq 20 \text{ \AA}$ in multiple fields. Green solid triangles show their luminosity function after they corrected it to allow for sources with fainter continuum magnitudes. Blue dotted curve shows the Schechter (1976) function fit to the Ly α luminosity function at $z = 0.194 - 0.44$ from Cowie et al. (2010). Red solid curve shows the fit at $z = 3.1$ from Gronwall et al. (2007). Red dashed curve shows the Gronwall et al. (2007) luminosity function with its normalization (ϕ_*) reduced by a factor of 30. This provides a reasonable match to the $z = 0.67 - 1.16$ luminosity function.

This confirms what was previously reported by Cowie et al. (2011). On the figure we also show the luminosity function they calculated for their 5 $\text{NUV} < 22$ pipeline extracted, optically confirmed, star-forming LAE galaxies from multiple fields with rest-frame $\text{EW}(\text{Ly}\alpha) \geq 20 \text{ \AA}$ (green open triangles). In addition, we show their luminosity function after they corrected it (green solid triangles) to allow for sources with fainter continuum magnitudes (see Deharveng et al. 2008 and Cowie et al. 2010 for details). Since many of the LAEs with Ly α luminosities $\sim 10^{43} \text{ erg s}^{-1}$ have $\text{NUV} > 22$, this correction is substantial. It is these corrected points that we should compare with the present luminosity function.

The $z = 0.67 - 1.16$ luminosity function presented here

needs to be corrected for contamination from any remaining unidentified AGNs, which will slightly lower the overall normalization. We postpone these corrections to a subsequent paper, where we will present LAE catalogs determined from data cube extractions of all the deepest *GALEX* grism fields, together with the optical spectroscopic follow-up necessary to remove the residual AGNs in the sample (I. Wold et al. 2012, in preparation). However, even allowing for this, we can see that there is a dramatic evolution in the luminosity function between $z \sim 0.3$ and $z \sim 0.9$ and that high-luminosity Ly α sources seen at still higher redshifts are already present at $z \sim 1$.

6. SUMMARY

In this paper, we described a new method for obtaining a flux-limited sample of LAEs from *GALEX* grism data. We showed how for intensively observed fields with large numbers of independent grism images we could construct three-dimensional (two spatial axes and one wavelength axis) data cubes from the grism images. We then constructed the data cube for the central region of the CDFS-00, the field with the deepest *GALEX* grism observations, and used it to carry out a search for emission-line objects.

We detected 28 new $z \sim 1$ LAEs in our data cube search of the CDFS-00. By comparing with the ECDFS X-ray data, existing optical spectroscopy, and deep *U*-band imaging, we determined that the bulk of our new LAEs are real and that the UV spectroscopic redshifts based on the Ly α identifications are reliable. In looking at the high-resolution *HST* images that are available for some of the LAEs in our new sample, as well as for some of the LAEs from the *GALEX* pipeline sample, we found that the sources classified as AGNs are dominated by compact nuclei, while the sources that appear to be star-forming galaxies are primarily resolved small blue galaxies, often with multiple components. One of our new LAEs is spatially resolved with a linear major-axis diameter of 120 kpc. This places it in the category of the giant Ly α blobs, though at the low end in terms of its Ly α luminosity.

The LAEs that had previously been found by the *GALEX* pipeline were limited by the pipeline magnitude limit of $\text{NUV}=22$, but the new LAEs extend to much fainter magnitudes. Moreover, they also have higher EWs, since for a given Ly α flux and redshift, the $\text{NUV}=22$ continuum cut corresponds to an EW, which becomes progressively lower as one moves to lower Ly α fluxes. The consequences of this are severe: the pipeline progressively misses more sources from a Ly α flux of $\sim 8 \times 10^{-15} \text{ erg cm}^{-2} \text{ s}^{-1}$ down to a Ly α flux of $\sim 2 \times 10^{-15} \text{ erg cm}^{-2} \text{ s}^{-1}$, at which point it misses nearly all of them.

Finally, we computed the CDFS-00 LAE galaxy luminosity function for the redshift interval $z = 0.67 - 1.16$ using both the very small sample of LAE galaxies from the pipeline sample of Cowie et al. (2011; 2 galaxies) and the larger sample of LAE galaxies from our data cube search. We confirmed a dramatic evolution in the luminosity function between $z \sim 0.3$ and $z \sim 1$.

In the future, we plan to undertake data cube searches on the other deep *GALEX* fields to obtain a much larger sample of $z \sim 1$ LAEs (I. Wold et al. 2012, in preparation). This will enable us to make a precise determination of the luminosity function at this redshift. We also plan to do

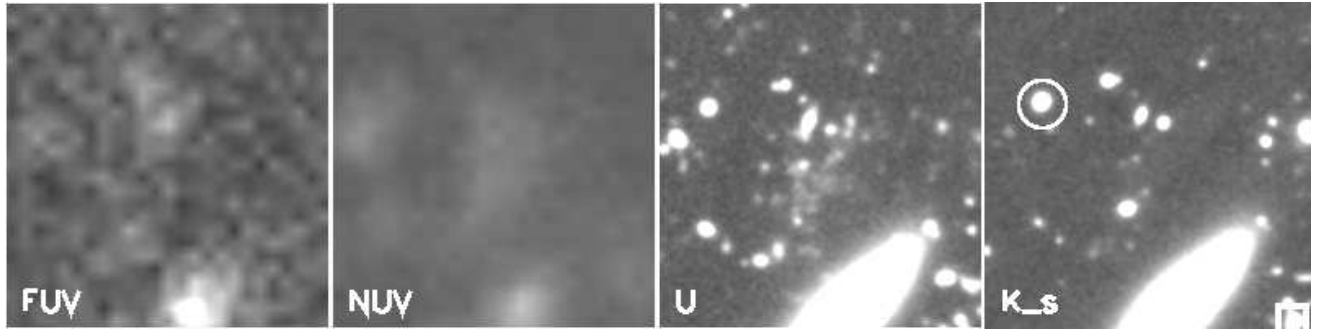


FIG. 14.— Images of the giant Ly α blob GALEX033246-274154. From left to right the panels show the FUV, NUV, VIMOS U (Nonino et al. 2009), and K_s images. Each thumbnail is $37'' \times 5$ on a side. In the final panel, we circle the nearest ($14''$) X-ray source in the ECDFS sample to the blob. This AGN is at $z = 0.740$ and hence cannot be the excitation source for the blob. We also mark with a square an AGN located $25''$ from the blob, whose redshift of $z = 0.982$ roughly matches that of the blob ($z = 0.977$).

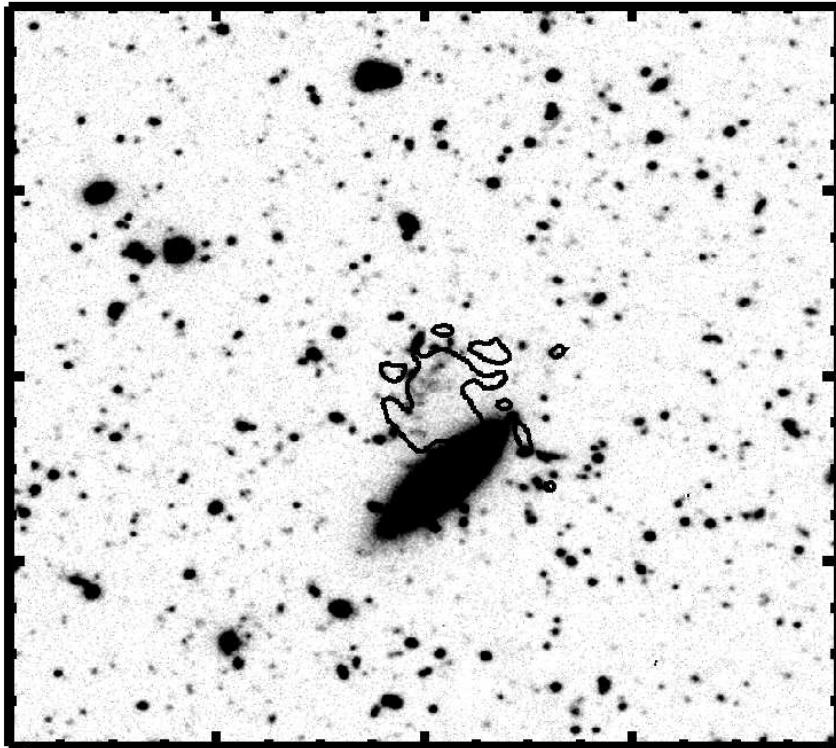


FIG. 15.— Contour of the Ly α emission-line region of the giant Ly α blob GALEX033246-274154 superimposed on the ultra-deep VIMOS U -band exposure of the area (Nonino et al. 2009). The emitter corresponds to an area of diffuse though structured continuum emission. Each large tick on the axes corresponds to an angular size of $30''$ or a linear size of 240 kpc at the $z = 0.977$ redshift of the object.

extensive optical spectroscopic follow-up to better assess the level of AGN contamination in the $z \sim 1$ LAEs.

We thank the referee for providing an interesting and thoughtful report that helped us to improve the paper. We thank Michael Cooper for supplying spectra from the Ari-

zona CDFS Environment Survey (ACES). We gratefully acknowledge support from the University of Wisconsin Research Committee with funds granted by the Wisconsin Alumni Research Foundation and the David and Lucile Packard Foundation (A. J. B.), as well as from NSF grant AST-0709356 (L. L. C.).

REFERENCES

- Atek, H., et al. 2009, *A&A*, 506, L1
 Balestra, L., et al. 2010, *A&A*, 512, 12
 Barger, A. J., Cowie, L. L., Brandt, W. N., Capak, P., Garmire, G. P., Hornschemeier, A. E., Steffen, A. T., & Wehner, E. H. 2002, 124, 1839
 Cooper, M. C., et al. 2012, *MNRAS*, submitted (arXiv:1112.0312)
 Cowie, L. L., Barger, A. J., & Hasinger, G. 2012, *ApJ*, in press (arXiv:1110.3326)
 Cowie, L. L., Barger, A. J., & Hu, E. M. 2010, *ApJ*, 711, 928
 Cowie, L. L., Barger, A. J., & Hu, E. M. 2011, *ApJ*, 738, 136
 Deharveng, J.-M., et al. 2008, *ApJ*, 680, 1072
 Felten, J. E. 1976, *ApJ*, 207, 700
 Finkelstein, S. L., Cohen, S. H., Malhotra, S., & Rhoads, J. E. 2009a, *ApJ*, 700, 276
 Finkelstein, S. L., et al. 2009b, *ApJ*, 703, L162
 Giacconi, R., et al. 2002, *ApJS*, 139, 369
 Giavalisco, M., et al. 2004, *ApJ*, 600, L93
 Grogin, N. A., et al. 2011, *ApJS*, 197, 35
 Gronwall, C., et al. 2007, *ApJ*, 667, 79
 Gwyn, S. D. J. 2008, *PASP*, 120, 212
 Horne, K. 1986, *PASP*, 98, 609
 Hornschemeier, A. E., et al. 2001, *ApJ*, 554, 742
 Hu, E. M., Cowie, L. L., & McMahon, R. G. 1998, *ApJ*, 502, L99
 Keel, W. C., White, R. E., Chapman S., & Windhorst, R. A. 2009, *AJ*, 138, 986
 Koekemoer, A. M., et al. 2011, *ApJS*, 197, 36
 Le Fèvre, O., et al. 2005, *A&A*, 439, 845
 Lehmer, B. D., et al. 2005, *ApJS*, 161, 21
 Luo, B., et al. 2008, *ApJS*, 179, 19
 Martin, D. C. 2005, *ApJ*, 619, L1
 Matsuda, Y., et al. 2011, *MNRAS*, 410, L13
 Mignoli, M., et al. 2005, *A&A*, 437, 883
 Morrissey, P., et al. 2007, *ApJS*, 173, 682
 Nonino, M., et al. 2009, *ApJS*, 183, 244
 Popesso, P., et al. 2009, *A&A*, 494, 443
 Prescott, M. K. M., et al. 2012, *ApJ*, submitted (arXiv:1111.0630)
 Rix, H.-W., et al. 2004, *ApJS*, 152, 163
 Scarlata, C., et al. 2009, *ApJ*, 704, 98
 Schechter, P. 1976, *ApJ*, 203, 297
 Shapley, A. E., Steidel, C. C., Pettini, M., & Adelberger, K. L. 2003, *ApJ*, 588, 65
 Silverman, J. D., et al. 2005, *ApJ*, 618, 123
 Silverman, J. D., et al. 2010, *ApJS*, 191, 124
 Straughn, A., et al. 2008, *AJ*, 135, 1624
 Szokoly, G. P., et al. 2004, *ApJS*, 155, 271
 Treister, E., et al. 2009, *ApJ*, 693, 1713
 Vanzella, E., et al. 2008, *A&A*, 478, 83
 Virani, S. N., Treister, E., Urry, C. M., & Gawiser, E. 2006, *AJ*, 131, 2373
 Xue, Y. Q., et al. 2011, *ApJS*, 195, 10

TABLE 1
EMISSION LINE SAMPLE

Name	R.A. (J2000.0)	Decl. (J2000.0)	NUV (AB)	FUV (AB)	z_{galex}	f (Ly α) (erg/cm ² /s)	$\log L$ (Ly α) (erg/s)	EW (Ly α) (Å)	UV Type	$\log f$ (2 – 8 keV) (erg/cm ² /s)	z_{ground}	Opt Type ^a
(1)	(2)	(3)	(4)	(5)	(6)	(7)	(8)	(9)	(10)	(11)	(12)	(13)
GALEX033112-281517	52.800373	-28.254972	23.19	27.56	1.160	77±3	43.16	109±2	
GALEX033359-275326	53.499123	-27.890778	22.14	24.11	1.144	24±3	43.45	82±4	AGN	
GALEX033301-273227	53.255127	-27.540943	23.64	-27.39	1.137	20±3	42.89	92±6	
GALEX033146-272942	52.942501	-27.495249	22.81	25.06	1.133	15±3	42.71	28±8	
GALEX033230-280804	53.125668	-28.134527	22.42	23.76	1.126	18±3	43.11	50±6	AGN	
GALEX033348-280216	53.453625	-28.037998	23.49	25.57	1.125	10±3	42.93	89±5	
GALEX033120-274917	52.837460	-27.821417	23.00	-29.55	1.116	13±2	42.76	38±5	
GALEX033255-281320	53.231544	-28.222471	22.51	28.98	1.084	14±3	42.80	28±5	
GALEX033200-274319	53.001377	-27.722055	22.45	24.24	1.042	10±3	43.11	61±7	...	-14.2	1.037 ^b	BLAGN
GALEX033228-273614	53.118168	-27.604000	23.69	25.77	1.033	41±2	42.59	58±6	...	ECDFS	...	
GALEX033113-274949	52.807587	-27.830278	22.54	-28.61	1.032	16±2	42.70	26±5	
GALEX033202-280320	53.010712	-28.055723	23.55	25.24	1.017	26±2	42.89	104±3	AGN	-13.7	1.014 ^c	Sy2
GALEX033111-275506	52.798542	-27.918472	24.00	-27.28	0.996	15±2	42.62	89±8	
GALEX033336-274224	53.402752	-27.706667	23.04	26.32	0.978	28±2	43.10	116±9	AGN	-14.7	...	
GALEX033246-274154 ^d	53.195625	-27.698416	23.41	25.82	0.977	14±2	42.86	93±3	...	ECDFS	...	
GALEX033204-273725	53.017002	-27.623806	22.87	24.31	0.976	8±3	43.14	107±8	AGN	-13.5	0.970 ^e	BLAGN
GALEX033335-273934	53.398125	-27.659584	22.62	23.31	0.949	9±2	42.85	47±6	...	-14.2	...	
GALEX033329-280127	53.373249	-28.024277	23.23	25.71	0.941	23±2	42.62	48±1	...	ECDFS	...	
GALEX033206-281408	53.026459	-28.235723	21.88	25.76	0.913	10±2	43.22	60±3	
GALEX033044-280237	52.686874	-28.043751	23.33	27.41	0.872	12±2	42.57	56±7	0.855	NELG
GALEX033251-280809	53.214336	-28.135973	22.76	26.13	0.836	39±2	42.67	44±0	0.832	NELG
GALEX033045-274506	52.689747	-27.751862	23.21	25.77	0.830	7±2	42.64	65±2	
GALEX033314-274834	53.310581	-27.809526	24.24	25.30	0.830	11±2	42.49	119±3	...	ECDFS	...	
GALEX033057-273316	52.739708	-27.554583	22.49	24.02	0.795	20±2	42.72	43±6	0.790	NELG
GALEX033124-275625	52.851665	-27.940474	22.78	25.39	0.775	9±2	42.62	48±9	...	ECDFS	0.776 ^f	NELG
GALEX033235-274059	53.148876	-27.683195	23.74	25.95	0.746	7±2	42.70	150±9	...	ECDFS	0.735 ^g	NELG
GALEX033146-274846	52.942459	-27.812805	23.18	25.48	0.742	19±2	42.78	107±3	...	ECDFS	...	
GALEX033131-273429	52.880333	-27.574804	22.57	25.54	0.695	8±1	43.21	191±8	...	-14.1	0.688 ^h	Sy2

^aBLAGN = broad-line AGN, i.e., presence of at least one emission line having FWHM > 2000 km s⁻¹; Sy2 = Seyfert 2, i.e., [NeV] emission; NELG = narrow emission-line galaxy, i.e., at least one emission line and no BLAGN signatures or [NeV] emission

^bSzokoly et al. (2004)

^cTreister et al. (2009)

^dGiant Ly α blob; see Figures 14 and 15

^eTreister et al. (2009); Szokoly et al. (2004) give $z = 0.977$

^fCooper et al. (2011)

^gVanzella et al. (2008)

^hSilverman et al. (2010)